

Two-electron one-photon transitions in Li-like ions

L. Natarajan

Department of Physics, University of Mumbai, Mumbai 400032, India

(Received 11 September 2013; published 27 November 2013)

The x-ray wavelengths and rates from double electron radiative transitions in Li isoelectronic sequences are evaluated for 17 ions with $14 \leq Z \leq 54$ using fully relativistic multiconfiguration Dirac-Fock wave functions in the active space approximation with the inclusion of finite nuclear size, Breit interaction, self-energy, and vacuum polarization. A detailed discussion on the anomalous mixing coefficients contributions to the $1s2s(^3S_1)3p^2P_{1/2}$ level for ions with $38 \leq Z \leq 43$ is given. The sensitivity of transition rates to the Breit interaction is also analyzed. The present results are compared with other available theoretical data. The errors associated with the transitions are highlighted for some of the strongest lines, taking into account the uncertainties on the fine-structure energy levels and also on the line strengths.

DOI: [10.1103/PhysRevA.88.052522](https://doi.org/10.1103/PhysRevA.88.052522)

PACS number(s): 31.30.Gs

I. INTRODUCTION

The x rays from the inner shell ionized few-electron systems provide valuable information on the temperature, density, and ionization state of the plasma and hence are useful in the theoretical modeling of plasmas. The data on the intercombination and electric dipole forbidden lines have been proven to be extremely useful in understanding the characteristics such as density fluctuations in hot astrophysical plasmas [1]. A detailed study of Capella spectra on the weak intercombination line of He-like Ne contaminated by the L lines from Li-like to Mg-like Fe is found to give valuable information on the Ne to Fe abundance ratio [2]. The energies and rates of $K\alpha$ x-ray satellites from highly charged few-electron ions have been investigated in laser-produced plasmas [3], tokamak plasmas [4–7], beam-foil spectroscopy [8–11], and electron beam ion traps [12,13]. The utility of $K\beta$ spectra as a diagnostic of the electron temperature of low-density plasmas has been reported by Beiersdorfer *et al.* [14] from the high-resolution measurements on Princeton Large Torus (PLT) tokamak. Investigations on the $K\beta$ x-ray emission from laser plasma [15] and electron beam ion traps (EBIT) [16] are also available. As the decay processes of an inner shell vacancy from highly charged few-electron ions are in general complex and the line assignment may be uncertain when clusters of lines are involved, it is necessary to have accurate atomic data on the positions and intensities of spectral lines from all possible modes of decay from a given charge state for a proper interpretation of nonequilibrium ionizing plasmas [17]. The Li-like $1s2l3l'$ satellite intensities have been shown to be sensitive to fluctuations in the electron density near the critical value for laser experiments [18]. While systematic relativistic and nonrelativistic calculations on the one-electron one-photon (OEOP) $K\alpha$ and $K\beta$ x-ray satellites from Li-like ions are available in the literature [19–23], calculations on other types of unusual transitions are limited [20,21]. While the OEOP lines are intense, two-electron one-photon (TEOP) transitions where both the electrons jump to the same inner shell are weak [24,25]. However, unlike this normal TEOP decay mode, special types of TEOP transitions where the two electrons make transitions to different shells are highly intense. The spectral features of these anomalous satellites have till recently been neglected in the interpretation of soft

x-ray spectra. However, such special types of transitions have been experimentally observed [17,26–28]. Gu *et al.* [17] have reported these unusual types of satellites in the K x-ray spectra of Li-like to C-like oxygen obtained with a reflection grating spectrometer on the EBIT. Order-of-magnitude-intense two-electron satellite transitions in laser-produced plasma experiments on He-like and Li-like Si have been recorded [26,27]. Elliott *et al.* [28] have investigated the overlap of spectral lines from transitions between $n = 3$ and $n = 2$ autoionizing states of Al^{10+} for a possible application in a photopumped x-ray lasing scheme.

We have recently reported our extensive investigation on the normal $K\beta$ x-ray satellites from $1s2s3p-1s^22s$ transitions in Li-like ions with $14 \leq Z \leq 54$ [23]. The goal of the present work is to analyze the relatively intense, less-explored satellite lines arising from the above referred special type of TEOP transitions. The correlation effects make the TEOP transitions interesting. They contaminate the OEOP transitions, whether weak or strong. In this work, an attempt is made to analyze the characteristics of the unusually high intense satellites from $1s2s3p-1s^23s$ and $1s^23d$ transitions and to stress the importance of these transitions in the radiative decay of Li-like ions. The branching ratios between the two types of radiative transitions are obtained. The calculations are carried out using multiconfiguration Dirac-Fock (MCDF) wave functions with the inclusion of Breit interaction, self-energy, and vacuum polarization. The finite nuclear size effect is included in the calculations by considering a two-parameter Fermi charge distribution. The correlation effects are computed by excitation of the atomic orbitals in the active space approximation. The calculations are carried out using GRASP2K code [29–31].

II. NUMERICAL PROCEDURE

In a multiconfiguration relativistic calculation, the configuration state functions (CSFs) are symmetry-adapted linear combinations of Slater determinants constructed from a set of one-electron Dirac spinors. A linear combination of these CSFs is then used in the construction of atomic state functions (ASFs) with the same J and parity:

$$\Psi_i(J^P) = \sum_{\alpha=1}^{n_{\text{CSF}}} c_{i\alpha} \Phi(\Gamma_{\alpha} J^P), \quad (1)$$

where $c_{i\alpha}$ are the mixing coefficients for the state i and n_{CSF} is the number of CSFs included in the evaluation of the ASFs. The Γ_α represents all the one-electron and intermediate quantum numbers needed to define the CSFs and the configuration mixing coefficients are obtained through the diagonalization of the Dirac-Coulomb Hamiltonian

$$\mathbf{H}_{\text{DC}} = \sum_i \left[c\alpha_i \cdot \mathbf{p}_i + (\beta - 1)c^2 - \frac{Z}{\mathbf{r}} \right] + \sum_{i>j} \frac{1}{\mathbf{r}_{ij}}. \quad (2)$$

Once a set of radial orbitals and the expansion coefficients are optimized for self-consistency, relativistic configuration interaction (RCI) calculations can be performed by including higher-order interactions in the Hamiltonian. The most important of these is the transverse photon interaction

$$\mathbf{H}_{\text{trans}} = \sum_{i,j}^N \left[\frac{\alpha_i \cdot \mathbf{p}_i \cos(\omega_{ij})}{\mathbf{r}_{ij}} + (\alpha_i \cdot \nabla_i)(\alpha_j \cdot \nabla_j) \frac{\cos(\omega_{ij}) - 1}{\omega_{ij}^2 \mathbf{r}_{ij}} \right], \quad (3)$$

where ω_{ij} is the wave number of the exchanged virtual photon and is obtained as the difference between the diagonal Lagrange multipliers associated with the orbitals. However, this is valid only when the shells are singly occupied and the diagonal energy parameters may not represent the correct binding energies of the orbitals in a variously ionized atomic system. Hence in the present work, the low-frequency limit $\omega_{ij} \rightarrow 0$ is considered and only the mixing coefficients are recalculated by diagonalizing the Dirac-Coulomb-Breit-Hamiltonian matrix. The dominant QED corrections comprise self-energy and vacuum polarization. While the former contribution is evaluated in the hydrogenlike approximation, the later correction is treated perturbatively. The theoretical background using relativistic wave functions and higher-order corrections is described in detail in the literature [31–33].

The generation of near-exact atomic state functions using systematic expansions of the orbitals in the active space has been discussed in our earlier studies [23–25,34]. In this method, the electrons from the occupied orbitals are excited to unoccupied orbitals in the active set. Since the orbitals with the same principal quantum number n have near similar energies, the active set is expanded in layers of n . While the initial states are the same for both sets of transitions, the final states come either from $1s^23s$ or from $1s^23d$ configurations, thereby leading to changes in the redistribution of the electron cloud. To account for a near-accurate description of atomic levels, we carried out separate calculations for each set of transitions and generated appropriate wave functions.

The correlation contribution was evaluated by considering single and double (SD) excitations of electrons from the occupied shells to unoccupied virtual shells. In the first step, with no excitation we generated monoconfiguration wave functions for the $1s2s3p$ and $1s^23s$ reference configurations in the extended optimal level (EOL) scheme using the variational method. In EOL calculations, the radial functions and the mixing coefficients are determined by optimizing the energy functional, which is the weighted sum of the energy values corresponding to a set of $(2j + 1)$ eigenstates. As this method is based on the simultaneous optimization of multiple levels

with a selected J , the significant interactions between neighboring levels can be determined to near accuracy. In the second step, we included limited configuration mixing by allowing SD excitations of electrons from the reference sets and generated 16 and 4 CSFs for the odd and even parity states, respectively. These optimized CSFs were then used to evaluate the transition parameters. In the third step, we included the $2p$ shell and generated CSFs through SD excitations. In this step, only the $2p$ orbital was variational and all the other CSFs were frozen to their preceding optimization values. In the fourth step, we considered the $3d$ orbitals and followed a procedure similar to that in the third step. Then, by gradually expanding the size of the active space in layers of n until the convergence and stability of the observable was obtained, the computations were repeated for each step-by-step multiconfiguration expansion, taking care of the convergence criterion on the orbitals (10^{-8}). As explained above, to ensure numerical stability and to reduce processing time, during each layer-by-layer expansion of the virtual orbitals, only the newly added orbitals were optimized, while the previously generated orbitals were kept frozen. The systematically expanded orbitals thus generated were used in the evaluation of MCDF transition energies and rates. In the subsequent RCI calculations, we included higher-order corrections and recalculated the mixing coefficients with a frozen radial set. A similar procedure was followed for the other set of $1s2s3p$ - $1s^23d$ transitions also. The ASFs thus generated were transformed to become biorthonormal before computing the transition rates. Our entire analysis on the effects of large configuration mixing together with Breit interaction and QED effects is carried out with respect to the limited orbital set generated from the SD excitations of electrons in the reference configuration.

As TEOP transitions are correlation dependent, to ensure that the most important correlation configurations are captured, the transition parameters were evaluated using the active set $\{nl, l \leq n - 2\}$, with $n = 1$ to 6 and extended to the $n = 7$ layer with spd symmetry. Further expansion of the active space did not contribute much to the mixing coefficients.

III. RESULTS AND DISCUSSION

In determining the accuracy of our computed data, we have considered a set of quality criteria such as optimization of the orbitals, convergence of the calculated term energies, comparison of the computed spectra with other available data, and agreement between the length and velocity forms of transition rates. In Table I, we study the convergence of the MCDF energy eigenvalues for the various fine-structure states of the $1s2s3p$ configuration of Li-like Fe with an increasing set of active space. Also given in the table are the RCI term energies that include additional corrections from Breit interaction and QED effects. The active set in column 1 gives the orbitals in the set. For example, $\{n3/2\}$ means that the set consists of all the orbitals with $n = 1$ to 3 and $l = 0$ to 2. All the energies listed in this table are bound-state negative values. It is seen from the table that the level energies converge well with $\{nl, l \leq n - 2\}$ set with $n = 1$ to 6. However, to make sure that even smaller contributions to mixing coefficients from further expansion are not left out, we included an additional layer with $n = 7$ consisting of spd symmetry and the total CSFs based

TABLE I. Energy eigenvalues in 10^3 eV of the fine-structure states of the $1s2s3p$ configuration of Li-like Fe for an increasing set of orbitals. All are bound-state negative energies.

Active set	$^4P_{1/2}$	$^4P_{3/2}$	$^4P_{5/2}$	$(^3S_1)^2P_{3/2}$	$(^3S_1)^2P_{1/2}$	$(^1S_0)^2P_{1/2}$	$(^1S_0)^2P_{3/2}$
DF	12.370 65	12.369 64	12.365 69	12.360 24	12.359 42	12.338 21	12.332 97
{ $n23p$ }	12.371 32	12.370 19	12.366 67	12.360 75	12.35956	12.337 74	12.33276
{ $n3l2$ }	12.371 61	12.370 70	12.366 79	12.365 21	12.365 00	12.340 77	12.335 34
{ $n4l3$ }	12.371 87	12.370 72	12.366 77	12.365 22	12.365 03	12.340 94	12.335 49
{ $n5l4$ }	12.371 91	12.371 03	12.367 06	12.365 57	12.365 39	12.341 42	12.335 86
{ $n6l4$ }	12.371 93	12.371 06	12.367 07	12.365 59	12.365 42	12.341 47	12.335 90
{ $n7l4$ }	12.371 93	12.371 06	12.367 08	12.365 60	12.365 43	12.341 48	12.335 90
RCI	12.366 79	12.366 34	12.362 40	12.360 95	12.360 38	12.335 88	12.330 32

on 39 relativistic subshells for the even and odd parity states are 6499.

In Table II, a comparison of our level energies with (RCI) and without (MCDF) higher-order corrections with respect to the $1s^22s^2S_{1/2}$ ground state of Li-like Ar is made with the data from the HULLAC code [14] and NIST compilation [35]. As the data recommended by NIST on the excitation energies of the various states of the $1s2s3p$ configuration of Li-like ions under consideration are available only for Ar, we have chosen Ar¹⁵⁺ for comparison. Our energies are in better agreement with the NIST compilation than with the HULLAC data calculated with parametric potential. Our energies in general differ from the HULLAC values by 0.1%. We find that the excitation energies with only correlation agree well with the NIST compilation with a respective difference of 0.2% and $\leq 0.02\%$ for the $1s^23s$ and $1s2s3p$ configurations. The RCI excitation energies are less than NIST values by 0.3% and 0.09%, respectively, for the final and initial fine-structure states. The differences are due to the fact that the theoretical excitation energies listed in the NIST database include a rough estimate of QED effects.

As explained in our previous paper [23], the energy ordering of the low-lying states of the $1s2s3p$ configuration does not follow a unique level scheme, and with increasing Z , the levels are influenced differently by correlation and higher-order

corrections. We especially notice an anomalous level structure for ions in the $38 \leq Z \leq 43$ region, and though the maximum contribution to the ASF describing the $1s2s3p_{3/2}$ $J = 1/2$ state should come from this state, it becomes only the second contributing state and we come across two $J = 1/2$ states instead of one. Naming them as levels I and II, we find an irregular variation in the contribution from the $1s2s3p_{3/2}$ $J = 1/2$ state to these two levels. The contribution is appreciable for a particular anomalous $J = 1/2$ state for certain ions in the range $38 \leq Z \leq 43$ while the trend changes for the other ions in this region and is more for the second level. In our earlier paper, out of the two $J = 1/2$ states, we considered only that state for which the contribution from the $1s2s3p_{3/2}$ $J = 1/2$ state was maximum. In this paper, we discuss in detail both the anomalous levels. For $Z \leq 37$ and $Z \geq 44$, the major contributions to the three $J = 1/2$ states come from the expected $1s2s(^1S_0)3p_{1/2}$, $1s2s(^3S_1)3p_{1/2}$, and $1s2s(^3S_1)3p_{3/2}$ states. While the correlation CSFs that contribute substantially to the mixing coefficients of the above-listed first two $J = 1/2$ states are mostly the same for all ions, the dominant correlation states that contribute to the $1s2s(^3S_1)3p_{3/2}$ $^2P_{1/2}$ state change for ions with $38 \leq Z \leq 43$. In this range, the major contribution to this state comes from the $J = 1/2$ state of either the $1s2p_{1/2}(^3P_0)3s$ configuration

TABLE II. Comparison of LSJ term energies in cm^{-1} for $1s2s3p$ and $1s^23s$ configurations of Li-like Ar with available data. Columns 2 and 3 list, respectively, the calculated excitation energies with only correlation (MCDF) and correlation coupled with higher-order corrections (RCI). Labels I to IV give the differences between our calculated and earlier results. I, MCDF and NIST; II, MCDF and HULLAC; III, RCI and NIST; and IV, RCI and HULLAC. All energies are displayed with respect to the Li-like ground state.

Levels	MCDF	RCI	NIST ^a	HULLAC ^b	Difference			
					I	II	III	IV
$1s^23s\ ^1S_0$	4 165 838	4 163 537	4 176 030		-10 192		-12 493	
$1s2s3p$								
$(^1S_0)^2P_{1/2}$	29 354 494	29 329 752	29 360 800	29 373 751	-6306	-19 257	-31 048	-43 999
$(^1S_0)^2P_{3/2}$	29 368 255	29 342 670	29 360 800	29 365 126	7455	3129	-18 130	-22 456
$(^3S_1)^2P_{1/2}$	29 215 521	29 189 098	29 213 300	29 226 093	2221	-10 572	-24 202	-36 995
$(^3S_1)^2P_{3/2}$	29 214 470	29 187 037	29 212 400	29 225 239	2070	-10 769	-25 362	-38 202
$^4P_{1/2}$	29 197 287	29 170 147		29 208 167	-4013	-10 880	-31 153	-38 020
$^4P_{3/2}$	29 199 502	29 171 409	29 201 300	29 210 726	-	-11 224	-	-39 317
$^4P_{5/2}$	29 205 180	29 176 815						

^aReference [35].

^bReference [14].

TABLE III. Mixing coefficients to the $1s2s(^3S_1)3p_{3/2}^2P_{1/2}$ state from the first four major contributing configuration states for various Z .

Z		$1s2s(^3S_1)3p_{3/2}$	$1s2p_{1/2}(^3P_0)3s$	$1s2s(^1S_0)3p_{1/2}$	$1s2p_{3/2}3s$	$1s2p_{1/2}(^3P_1)3s$
26		0.8869	0.3348		-0.1941	0.1578
36		0.7231	0.6522	0.1738	-0.0946	
38	I	0.6609	0.7199	0.1777	-0.0713	
	II	0.5503	-0.5465		-0.1547	0.6082
39	I	0.6026	0.7704	0.1816	-0.0574	
	II	0.5908	-0.4700	0.0540	-0.1538	0.6362
40	I	0.5470	0.8102	0.1830		-0.0521
	II	0.6136	-0.3992	-0.0806	-0.1509	0.6564
42	I	0.4363	0.8670	0.1874	-0.1082	
	II	0.6121	-0.2648		-0.1467	0.7058
44		0.9429	-0.2940	-0.0966	-0.0820	
50		0.8812	-0.3720	-0.2290	-0.1703	
54		0.8349	-0.4618	-0.2694	-0.1190	

or the $1s2p_{1/2}(^3P_1)3s$ configuration, and the expected $J = 1/2$ state from $1s2s(^3S_1)3p_{3/2}$ becomes the second major contributor in both the cases. This gives rise to two states, one from $1s2p_{1/2}(^3P_0)3s$ and the other from $1s2p_{1/2}(^3P_1)3s$ for the same $1s2s(^3S_1)3p_{3/2}^2P_{1/2}$ state. For example, for $Z = 38$, the contributions from the $1s2s3p_{3/2}^2P_{1/2}$ state to levels I and II are 43.7% and 30.3%, respectively, while for $Z = 42$, the correlation effect flips and we get 19% and 37.5% for the respective I and II levels. The main correlation states are also not the same in both the cases. It is $1s2p_{1/2}(^3P_0)3s$ for $Z = 38$, whereas for $Z = 42$, it is $1s2p_{1/2}(^3P_1)3s$. The energy difference between the two LSJ states is also marginal. For Li-like Mo, we find that the energy differences between these two states are 10 and 14 eV with and without higher-order corrections. The reduction in the expected number of $1s2s3p^2P_{1/2}$ states from three to two and the additional unexpected states coming from the $1s2p3s$ configuration suggest that strong configuration mixing between $2p$ and $3s$ states shuffles the ordering of energy levels leading to probable violation of the level scheme prediction in this region. In effect, levels I and II reveal that the most probable locations of the electrons in the $2s$ and $3p$ shells are hampered by correlation, and differences between levels I and II are due to the differences in the spatial distribution of the two electrons that are severely affected by configuration mixing.

To elaborate on this, we give in Table III, the mixing coefficients to the $1s2s(^3S_1)3p_{3/2}^2P_{1/2}$ state from the first four major contributing states for various Z . It is seen from the table that for level I, the maximum contribution to the $1s2s(^3S_1)3p_{3/2}^2P_{1/2}$ state comes from $1s2p_{1/2}(^3P_0)3s$, whereas for level II, it comes from $1s2p_{1/2}(^3P_1)3s$. Since the state under consideration is $(^3S_1)^2P_{1/2}$ and depending on for which level (I or II) there is a larger contribution from this state, we notice that, for $Z = 38$ and 39 , level I should be taken into account, while for $Z = 40$ and 42 , it is level II that represents the $(^3S_1)^2P_{1/2}$ state. The differences in the correlation can thus be well attributed to the differences in how the electrons distribute themselves spatially. In Fig. 1, the percentage mixing coefficient contribution to the $J = 1/2$ state from $1s2s(^3S_1)3p_{3/2}$ is shown for various Z . It is clear from the figure that the interplay between correlation and

higher-order corrections leads to an anomalous level structure and prevents unique identification of the $(^3S_1)^2P_{1/2}$ state for ions with $Z = 38$ to 43 .

Figure 2 gives sample plots of the contributions from Breit interaction and QED effects to the energies of the $1s^23s^2S_{1/2}$ state and the $^4P_{1/2}$, $(^1S_0)^4P_{3/2}$, and $(^1S_0)^2P_{1/2}$ states of the $1s2s3p$ configuration. The higher-order corrections decrease the photon energy, and at $Z = 54$, the contributions from these correction terms lower the MCDF transition energy by 100 eV.

In Fig. 3, the ratios of length to velocity rates of $1s2s3p-1s^23s$ transitions are illustrated. The figure shows a good agreement between the two rates and the ratios range from 0.99 to 1.01. The general trend of the curve with marginal variations in the length and velocity forms justifies the expected necessary condition and also gauges the level of accuracy of our computation.

In Tables IV and V, respective comparisons of our RCI wavelengths and length gauge rates for $1s2s3p-1s^23s$ transitions with the available SUPERSTRUCTURE values of Bely-Dubau *et al.* [20] and relativistic EAL data of Chen [21] are made. Our MCDF-EOL rates for $Z = 26$ and 30 are also included for the sake of comparison. For $Z = 38$ to 42 , the

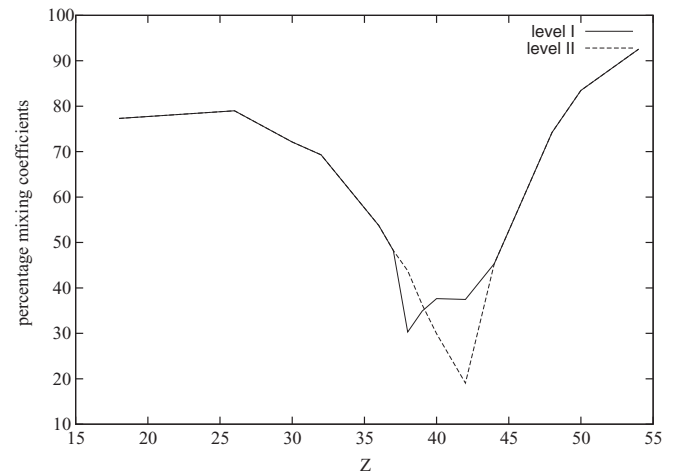


FIG. 1. Mixing coefficient contribution in percent from the $(^3S_1)^2P_{1/2}$ state for levels I and II.

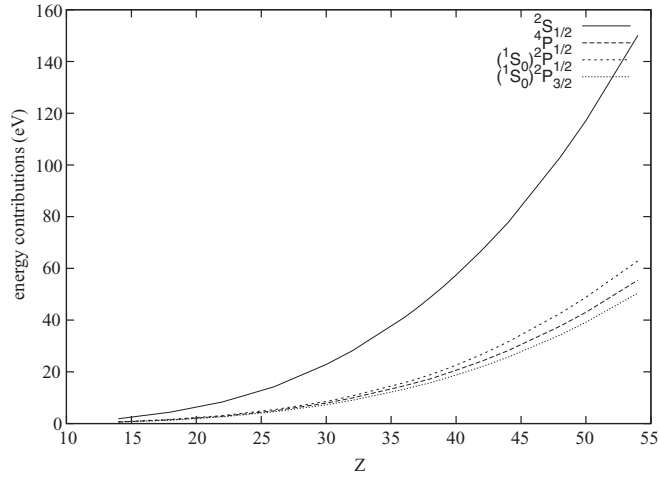


FIG. 2. Energy contributions from Breit + QED corrections to the $1s^23s$ ($^2S_{1/2}$) state and the $1s2s3p$ ($^4P_{1/2}$), $(^1S_0) 2P_{1/2}$, and $(^1S_0) 2P_{3/2}$ states.

rates from levels I and II are also reported. It may be noted that the present usage of LSJ notation to classify states is not rigorous except for low Z ions. Our RCI energies for Li-like Fe are in fairly good agreement with SUPERSTRUCTURE values [20]. Except for $Z = 14$ and 18, we find an excellent agreement between our calculated and EAL wavelengths [21]. We find better agreement between our MCDF-EOL and SUPERSTRUCTURE rates than with RCI rates. The present rates

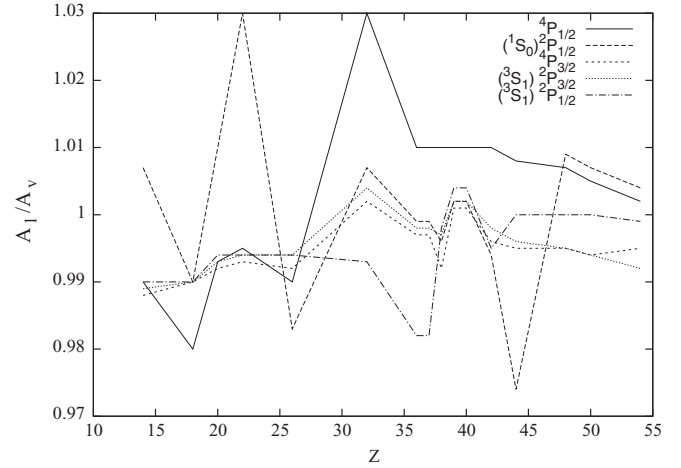


FIG. 3. Ratios of length to velocity forms of RCI rates for various $1s2s3p-1s^23s$ transitions.

are in good agreement with the EAL rates of Chen [21] for certain transitions and deviate for other transitions. Our MCDF-EOL rates for Fe^{23+} and Zn^{27+} compare better with EAL values [21] than with RCI rates, especially for transition from the $(^1S_0) 2P_{1/2}$ state. The large correlation configurations along with the EOL scheme considered in this work might account for the deviations between our RCI and earlier data. For ions in the range $38 \leq Z \leq 44$, the transition rates exhibit peculiar variations. The transition rate from $(^1S_0) 2P_{3/2}$ shows a minimum at $Z = 39$ and increases sharply by 3 orders of

TABLE IV. RCI wavelengths in \AA of the $1s2s3p-1s^23s$ transitions from Li-like ions. Also included are the available SUPERSTRUCTURE [20] and MCDF [21] wavelengths.

Z		$(^1S_0) 2P_{1/2}$	$(^1S_0) 2P_{3/2}$	$(^3S_1) 2P_{1/2}$	$(^3S_1) 2P_{3/2}$	$^4P_{1/2}$	$^4P_{3/2}$
14		6.6970	6.6960	6.7444	6.7448	6.7483	6.7481
	Ref. [21]	6.6977	6.6967	6.7438	6.7441	6.7479	6.7474
18		3.9739	3.9727	3.9964	3.9967	3.9992	3.9990
	Ref. [21]	3.9781	3.9720	3.9945	3.9945	3.9971	3.9969
20		3.1952	3.1939	3.2109	3.2112	3.2132	3.2130
22		2.6247	2.6234	2.6364	2.6366	2.6384	2.6382
	Ref. [21]	2.6248	2.6214	2.6362	2.6364	2.6382	2.6381
26		1.8605	1.8590	1.8672	1.8674	1.8690	1.8689
	Ref. [20]	1.8597	1.8582	1.8660	1.8661	1.8678	1.8676
	Ref. [21]	1.8605	1.8590	1.8671	1.8672	1.8689	1.8688
30		1.3859	1.3843	1.3899	1.3901	1.3916	1.3915
	Ref. [21]	1.3859	1.3843	1.3898	1.3900	1.3915	1.3914
32		1.2136	1.2120	1.2169	1.2170	1.2185	1.2184
36		0.9521	0.9505	0.9541	0.9542	0.9556	0.9555
	Ref. [21]	0.9520	0.9504	0.9539	0.9540	0.9554	0.9554
37		0.8998	0.8982	0.9016	0.9017	0.9030	0.9030
38		0.8516	0.8500	0.8531	0.8532	0.8546	0.8546
39		0.8071	0.8056	0.8086	0.8086	0.8100	0.8099
40		0.7660		0.7668	0.7674	0.7686	0.7686
42		0.6925	0.6909	0.6931	0.6928	0.6948	0.6948
	Ref. [21]	0.6924	0.6909	0.6930	0.6926	0.6947	0.6947
44		0.6288	0.6273	0.6286	0.6290	0.6309	0.6390
48		0.5248	0.5233	0.5245	0.5247	0.5265	0.5265
50		0.4820	0.4805	0.4816	0.4818	0.4835	0.4835
54		0.4140	0.4088	0.4098	0.4099	0.4116	0.4116

TABLE V. RCI length gauge rates in s^{-1} of the $1s2s3p-1s^23s$ transitions. The earlier SUPERSTRUCTURE [20] and MCDF-EAL [21] rates are also listed. For the sake of comparison, sample MCDF-EOL rates for $Z = 26$ and 30 are also included. The values from the two anomalous (3S_1) $^2P_{1/2}$ states for $38 \leq Z \leq 43$ are represented by the symbols I and II, respectively. The numbers in the parentheses are powers of 10.

Z		$(^1S_0)^2P_{1/2}$	$(^1S_0)^2P_{3/2}$	$(^3S_1)^2P_{1/2}$	$(^3S_1)^2P_{3/2}$	$^4P_{1/2}$	$^4P_{3/2}$
14		6.348(11)	1.355(12)	3.954(11)	5.074(11)	1.560(9)	1.011(10)
	Ref. [21]	5.44(11)	1.06(12)	4.62(11)	5.84(11)	1.5(9)	9.1(9)
18		4.266(11)	4.428(12)	1.201(12)	1.971(12)	7.487(9)	8.451(10)
	Ref. [21]	7.41(11)	3.41(12)	1.12(12)	1.82(12)	7.71(9)	8.5(10)
20		4.632(11)	6.441(12)	1.298(12)	2.687(12)	1.109(10)	2.007(11)
22		1.088(11)	8.719(12)	1.583(12)	4.279(12)	1.231(10)	3.903(11)
	Ref. [21]	2.39(11)	7.11(12)	1.79(12)	4.6(12)	1.33(10)	3.83(11)
26		1.204(12)	1.067(13)	1.797(12)	1.039(13)	3.590(9)	1.130(12)
	MCDF-EOL	4.508(11)	8.520(12)	1.857(12)	9.955(12)	4.687(9)	9.669(11)
	Ref. [20]	2.8(11)	9.17(12)	2.09(12)	1.083(13)	1.6(10)	1.27(12)
	Ref. [21]	3.74(11)	8.49(12)	2.06(12)	1.08(13)	8.66(9)	1.13(12)
30		1.890(13)	7.366(12)	1.305(12)	2.758(13)	1.168(10)	2.528(12)
	MCDF-EOL	9.991(12)	6.179(12)	1.560(12)	2.610(13)	7.404(9)	2.615(12)
	Ref. [21]	5.68(12)	5.20(12)	1.66(12)	2.55(13)	4.53(9)	2.58(12)
32		3.253(13)	5.362(12)	1.428(12)	4.392(13)	3.665(10)	3.991(12)
36		6.494(13)	1.089(12)	1.223(12)	1.155(14)	2.419(11)	7.551(12)
	Ref. [21]	2.66(13)	3.71(11)	7.92(11)	1.04(14)	2.31(11)	6.76(12)
37		7.800(13)	6.033(11)	1.368(12)	1.491(14)	3.689(11)	8.525(12)
38	I	6.849(13)	1.823(11)	9.265(11)	1.835(14)	5.778(11)	8.664(12)
	II			1.933(14)			
39	I	7.815(13)	6.542(10)	3.613(12)	2.497(14)	7.053(11)	1.078(13)
	II			2.348(14)			
40	I	8.041(13)	3.492(14)	7.141(12)	3.248(14)	9.036(11)	1.236(13)
	II			2.894(14)			
42	I	4.294(13)	1.309(11)	2.568(13)	3.480(14)	1.340(12)	1.602(13)
	II			4.276(14)			
	Ref. [21]	1.26(13)	4.53(11)	4.09(14)	3.62(14)	1.18(12)	1.44(13)
44		4.667(12)	4.337(11)	5.405(14)	3.004(14)	2.007(12)	2.032(13)
48		5.967(13)	1.253(12)	4.237(14)	1.953(14)	3.682(12)	3.153(13)
50		1.106(14)	1.589(12)	3.232(14)	1.551(14)	4.981(12)	3.773(13)
54		2.072(14)	2.185(12)	1.980(14)	1.037(14)	7.600(12)	5.531(13)

magnitude for $Z = 40$. The intensity of the x-ray photon from the $(^3S_1)^2P_{3/2}$ state increases with Z , reaches a maximum at $Z = 42$, and decreases beyond this. The rate from the $(^3S_1)^2P_{1/2}-^2S_{1/2}$ transition shows an irregular variation, peaks at $Z = 44$, and then the line intensity decreases. The increase is sharp for level II, whereas the smooth increase shows up at $Z = 44$ for level I. The $(^1S_0)^2P_{1/2}-^2S_{1/2}$ rate in general increases with Z except for an irregular behavior around $Z = 38$ to 44. The spin-forbidden line intensity from the $^4P_{1/2}$ state dips to a minimum at $Z = 26$ and beyond this its intensity slowly increases. The $^4P_{1/2}-^2S_{1/2}$ transition is weak for all ions. However, the spin-forbidden transition from $^4P_{3/2}$ starts as a weak transition, its intensity increases with Z and becomes stronger than the allowed transition from the $(^1S_0)^2P_{3/2}$ state.

In Fig. 4, we analyze the effects of Breit and QED contributions on the length gauge RCI rates. Breit interaction has quite different effects on different individual transitions. For certain Z , these effects on some transitions are significant. For the others, they introduce very small deviations. The Breit interaction enhances the rates of some allowed transitions and reduces the rates of others. For $Z \leq 26$, the Breit interaction reduces the spin-forbidden rate from the $^4P_{1/2}$ state. For other ions, it enhances the rates. However, the higher-order

corrections enhance the $^4P_{3/2}-^2S_{1/2}$ transition rates for all ions and its contribution to both the rates are nearly the same. We find that the influence of these correction terms is transition

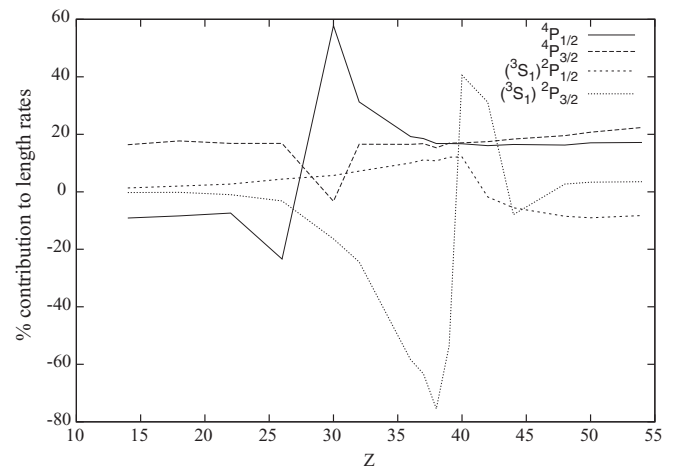


FIG. 4. Percentage contribution from Breit + QED corrections to length rates of various $1s2s3p-1s^23s$ transitions.

TABLE VI. Comparison of RCI wavelengths in Å and length gauge rates in s^{-1} of intense $1s2s3p-1s^23d$ transitions with the earlier data [20,21]. B and C refer to Bely-Dubau *et al.* [20] and Chen [21]. The values from the two anomalous (3S_1) $^2P_{1/2}$ states for $Z = 39, 40$, and 42 are represented by the symbols I and II, respectively. The numbers in the parentheses are powers of 10.

Z	$1s2s(^1S_0)3p$						$1s2s(^3S_1)3p$					
	$^2P_{1/2}-^2D_{3/2}$		$^2P_{3/2}-^2D_{3/2}$		$^2P_{3/2}-^2D_{5/2}$		$^2P_{1/2}-^2D_{3/2}$		$^2P_{3/2}-^2D_{5/2}$		$^4P_{3/2}-^2D_{5/2}$	
	Energy	Rate										
14	6.7316	1.07(12)	6.7306	1.08(11)	6.7309	9.69(11)	6.7810	1.14(10)	6.7857	6.21(9)	6.7821	1.75(8)
C	6.7313	9.53(11)	6.7303	9.39(10)	6.7306	8.61(11)	6.7779	8.3(9)	6.7785	4.21(9)	6.7813	1.63(8)
18	3.9900	2.87(12)	3.9888	2.94(11)	3.9892	2.65(12)	4.0129	3.74(10)	4.0135	1.02(10)	4.0150	2.12(9)
C	3.9898	2.61(12)	3.9887	2.56(11)	3.9890	2.35(12)	4.0114	3.02(10)	4.0120	7.44(9)	4.0133	1.97(9)
22	2.6347	5.93(12)	2.6333	6.33(11)	2.6337	5.81(12)	2.6468	1.03(11)	2.6474	7.68(9)	2.6482	1.39(10)
26	1.8673	1.01(13)	1.8657	1.19(12)	1.8661	1.10(13)	1.8742	2.41(11)	1.8745	2.92(8)	1.8752	6.01(10)
C	1.8670	9.42(12)	1.8655	1.0(12)	1.8660	9.6(12)	1.8737	2.23(11)	1.8742	3.74(8)	1.8746	5.53(10)
B	1.8663	8.86(12)	1.8648	1.07(12)	1.8652	9.82(12)	1.8727	2.40(11)	1.8732	4.34(8)		
28	1.6029	1.25(13)	1.6013	1.66(12)	1.6017	1.47(13)	1.6083	3.87(11)	1.6088	4.82(8)	1.6092	1.10(11)
32	1.2177	1.72(13)	1.2161	3.09(12)	1.2166	2.42(13)	1.2210	8.51(11)	1.2215	2.07(10)	1.2217	3.06(11)
36	0.9555	2.12(13)	0.9539	5.40(12)	0.9543	3.59(13)	0.9575	1.69(12)	0.9580	7.49(10)	0.9581	6.91(11)
C	0.9554	2.03(13)	0.9538	3.87(12)	0.9543	3.0(13)	0.9573	1.57(12)	0.9579	6.71(10)	0.9579	6.27(11)
37	0.9030	2.21(13)	0.9014	6.52(12)	0.9018	3.97(13)	0.9048	2.04(12)	0.9053	8.11(10)	0.9053	8.21(11)
39	I 0.8101	2.37(13)	0.8085	8.67(12)	0.8089	4.66(13)	0.8115	2.68(12)	0.8120	9.41(10)	0.8120	1.13(12)
II							0.8110	2.87(11)				
40	I 0.7689	2.44(13)	0.7673	9.53(12)	0.7677	4.97(13)	0.7697	2.94(12)	0.7707	9.83(10)	0.9053	9.84(10)
II							0.7701	5.3(11)				
42	I 0.6951	2.54(13)	0.6936	1.25(13)	0.6940	5.69(13)	0.6962	3.29(12)	0.6956	1.55(12)	0.6965	1.74(12)
II							0.6957	1.73(12)				
C	0.6951	2.33(13)	0.6936	7.84(12)	0.6940	4.65(13)	0.6957	1.06(12)	0.6958	1.13(11)	0.6964	1.56(12)
44	0.6313	2.54(13)	0.6298	1.73(13)	0.6303	6.48(13)	0.6311	1.73(11)	0.6320	1.87(12)	0.6324	2.22(12)
48	0.5271	2.26(13)	0.5256	2.92(13)	0.5261	7.88(13)	0.5268	1.46(11)	0.5275	2.64(12)	0.5278	3.41(12)
50	0.4843	2.09(13)	0.4827	3.65(13)	0.4832	8.44(13)	0.4839	9.07(10)	0.4845	3.06(12)	0.4847	4.05(12)
54	0.4094	1.89(13)	0.4109	6.79(13)	0.4114	9.58(13)	0.4119	3.72(9)	0.4125	3.94(12)	0.4126	5.46(12)

and Z dependent and this non-monotonic behavior of the intensities due to Breit interaction may well be attributed to the differences in mixing coefficients that are reevaluated in RCI calculations

In Table VI, we compare the wavelengths and rates of intense $1s2s3p-1s^23d$ transitions with those of Chen [21]. The SUPERSTRUCTURE data of Bely-Dubau *et al.* [20] for Fe^{23+} are also listed for comparison. The RCI energies and rates are in fairly good agreement with those of Bely-Dubau *et al.* [20]. As noticed in the $1s2s3p-1s^23s$ transitions, our wavelengths compare exceedingly well with the MCDF-EAL values [21] except for some marginal difference in the values of Si^{11+} and Ar^{15+} . The present rates also compare well with the EAL rates.

Sample plots for some allowed $E1$ rates from $1s2s3p-1s^23d$ transitions with only correlation and also with additional higher-order corrections are shown in Fig. 5. Similar plots for spin-forbidden rates are shown in Fig. 6. It is seen from the figures that Breit and QED corrections enhance the allowed rates and reduce the spin-forbidden rates.

While Tables II and comparisons of our computed values with the existing data [20,21], especially with the MCDF values of Chen [21], indicate the accuracy of our results, as a further assessment we have tried to critically evaluate the uncertainty in our RCI rates in terms of line strengths and transition energies. With ultrasensitive detectors, the experimental measurements of the photon energies can be more precise than those of the calculated energies and the computed rates

can be improved by using measured values. However, data on experimental transition energies are nonexistent for the ions under consideration and theoretical excitation energies are also listed in the NIST compilation [35] only for a few states of Li-like Ar and Fe. Hence we have estimated the relative errors in our calculated data with available excitation

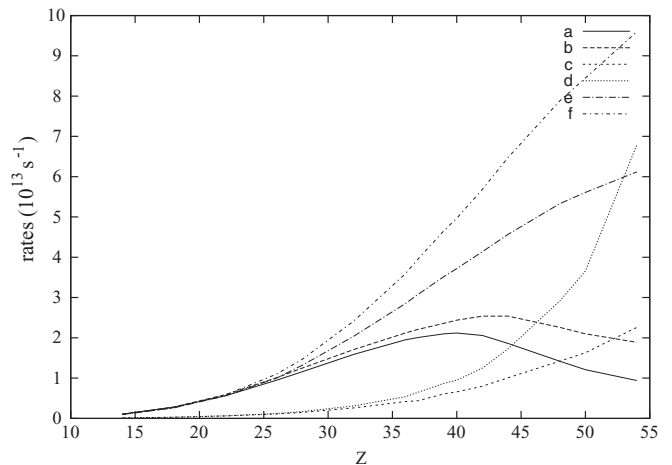


FIG. 5. MCDF and RCI rates from $1s2s(^1S_0)3p-1s^23d$ allowed transitions. Curves a, c, and e are rates with only correlation, while curves b, d, and f are rates with correlation and Breit interaction. a and b: $^2P_{1/2}-^2D_{3/2}$; c and d: $^2P_{3/2}-^2D_{3/2}$; e and f: $^2P_{3/2}-^2D_{5/2}$.

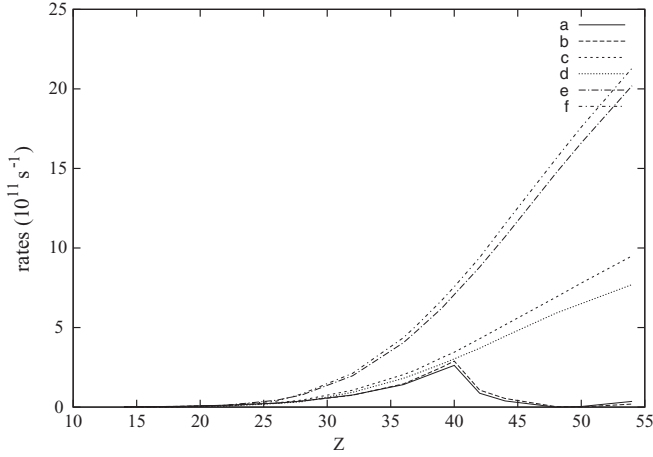


FIG. 6. MCDF and RCI rates from $(^3S_1) 2P_{3/2}-2D_{3/2}$, $4P_{1/2}-2D_{3/2}$, and $4P_{3/2}-2D_{3/2}$ transitions. Curves a, c, and e are rates with only correlation, while curves b, d, and f are rates with correlation and Breit interaction. a and b: $2P_{3/2}-2D_{3/2}$; c and d: $4P_{1/2}-2D_{3/2}$; e and f: $4P_{3/2}-2D_{3/2}$.

energies listed for Ar^{16+} and Fe^{24+} . For Si^{12+} and Ar^{16+} , we have also considered a mix of experimental [13,14] and NIST compiled excitation energies to evaluate experimental wavelengths. These wavelengths have subsequently been used in the transition rate calculations. While δE is the uncertainty in the photon energy, the uncertainties δS in the length (S_l) or velocity (S_v) forms of line strengths are calculated relative to the average of S_l and S_v . With A as the rate calculated using the NIST or experimental data and computed line strengths, the uncertainty in our RCI rate is (δA). In calculating A' , we have used the average of S_l and S_v . The uncertainty estimates δE , δS , and δA are listed in Table VII for the $E1$ lines from $1s2s3p-1s^23s$ transitions. The convergence of the line strengths along with the good agreement of the wavelengths testifies to the accuracy of our results. The relative error in the transition energies is within 0.005% and the relative difference in the length and velocity forms of line strengths is within a fraction of a percent.

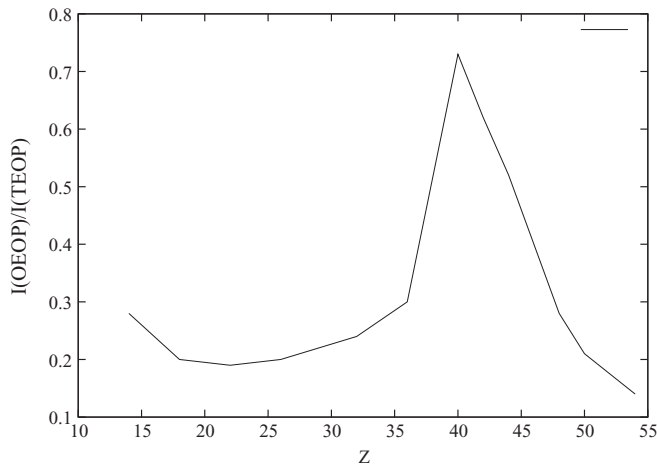


FIG. 7. Intensity ratios of OEOP and TEOP transitions from states of $1s2s3p$ configurations of Li-like ions.

TABLE VII. The errors in computed wavelengths, line strengths, and rates for electric dipole $1s2s3p-1s^23s$ transitions. $\delta\lambda$ listed for each element corresponds to the wavelength difference between our computed and NIST [35] data or experimental [14,15] data coupled with NIST data. δS gives the percentage deviation in the length and velocity form line strengths relative to the average of S_l and S_v , and δA is the percentage error between the RCI rates in length form and the energy scaled rates calculated with the average of S_l and S_v . The superscripts a and b indicate the experimental contributions for Si^{11+} [15] and Ar^{13+} [14], respectively. The numbers within the parentheses denote powers of 10.

Property	% Error				
	$1s2s(^1S_0)3p$		$1s2s(^3S_1)3p$		$4P_{3/2}$
	$2P_{1/2}$	$2P_{3/2}$	$2P_{1/2}$	$2P_{3/2}$	
$Z = 14$					
$\delta\lambda^a$	+4.8(-3)	+3.8(-3)	+4.1(-3)	+4.4(-3)	
δS	+7.0(-1)	+1.2(-1)	-1.0(-2)	-9.7(-1)	
δA^a	-2.2(-1)	-9.5(-1)	-3.5(-1)	+9.3(-1)	
$Z = 18$					
$\delta\lambda^b$	+3.3(-3)	+2.1(-3)	+3.2(-3)	+3.5(-3)	
$\delta\lambda$	+3.2(-3)	+2.0(-3)	+2.3(-3)	+2.5(-3)	+3.2(-3)
δS	+1.3(-1)	+9.7(-1)	+7.3(-1)	+9.1(-1)	+5.6(-1)
δA^b	-2.1(-1)	4.1(-1)	-2.5(-1)	-1.11	
δA	-2.1(-1)	1.1(-1)	-1.4(-1)	-1.07	-4.7(-2)
$Z = 26$					
$\delta\lambda$	-1.7(-3)		-1.3(-3)		
δS	-1.75	-1.5(-1)	-5.1(-1)	-2.6(-1)	
δA	-9.9(-1)			-1.0(-1)	

In Fig. 7, the intensity ratios of the $1s2s3p-1s^22s$ transitions [23] to the TEOP transitions considered in this work are plotted for various Z . The ratio between the two types of transitions slowly increases with Z , peaks at $Z = 40$, and then decreases.

IV. CONCLUSION

A comprehensive study of single-photon emission from double-electron jumps in Li isoelectronic sequences is carried out in RCI formalism. It is interesting to conclude that the peculiar TEOP decay due to strong electron correlation becomes a competitive channel to the regular OEOP transition. The calculated results are supplemented with error estimates wherever possible. The influence of Breit interaction on the transition rates is analyzed in detail. The study reveals strong and irregular variations of the deexcitation properties of the states along the Li isoelectronic sequence and this investigation can act as a challenging ground in understanding the interplay between electron-electron correlation and QED effects. To the best of our knowledge, no experimental data are available for the type of transitions considered in this work. Availability of such data from observations and measurements could help in judging the relative importance of this unusual type of TEOP transition and also in checking the theoretically predicted anomalous level structure of some mid Z ions.

ACKNOWLEDGMENTS

The author acknowledges the support from the Department of Science and Technology, Government of India, under Project No. SR/S2/LOP-5/2012.

- [1] E. Trabert, P. Beiersdorfer, G. Gwinner, E. H. Pinnington, and A. Wolf, *Phys. Rev. A* **66**, 052507 (2002).
- [2] J.-U. Ness, N. S. Brickhouse, J. J. Drake, and D. P. Huenemörder, *Astrophys. J.* **598**, 1277 (2003).
- [3] V. A. Boiko, A. Ya Faenov, S. A. Pikuz, I. Yu Skobelev, A. V. Vinogradov, and E. A. Yokov, *J. Phys. B* **10**, 3387 (1977).
- [4] M. Bitter, H. Hsuan, V. Decaux, B. Grek, K. W. Hill, R. Hulse, L. A. Kruegel, D. Johnson, S. von Goeler, and M. Zarnstorff, *Phys. Rev. A* **44**, 1796 (1991).
- [5] A. J. Smith, M. Bitter, H. Hsuan, K. W. Hill, S. von Goeler, J. Timberlake, P. Beiersdorfer, and A. Osterheld, *Phys. Rev. A* **47**, 3073 (1993).
- [6] P. Beiersdorfer, M. Bitter, D. Hey, and K. J. Reed, *Phys. Rev. A* **66**, 032504 (2002).
- [7] J. E. Rice, M. A. Graf, J. L. Terry, E. S. Marmor, K. Geising, and F. Bombarda, *J. Phys. B* **28**, 893 (1995).
- [8] E. Biémont, P. Quinet, A. Ya Faenov, I. Skobelev, J. Nilsen, V. M. Romanova, M. Scholz, L. Karpinski, and A. Szydlowski, *Phys. Scr.* **61**, 555 (2000).
- [9] J. P. Mosnier, R. Barchewitz, M. Cukier, R. Dei-cas, C. Senemaud, and J. Bruneau, *J. Phys. B* **19**, 2531 (1986).
- [10] A. Langenberg, R. L. Watson, and J. R. White, *J. Phys. B* **13**, 4193 (1980).
- [11] M. R. Tarbutt, R. Barnsley, N. J. Peacock, and J. D. Silven, *J. Phys. B* **34**, 3979 (2001).
- [12] S. B. Utter, P. Beiersdorfer, and E. Trabert, *Can. J. Phys.* **80**, 1503 (2002).
- [13] Y. Podpaly, J. Clementson, P. Beiersdorfer, J. Williamson, G. V. Brown, and M. F. Gu, *Phys. Rev. A* **80**, 052504 (2009).
- [14] P. Beiersdorfer, A. L. Osterheld, T. W. Phillips, M. Bitter, K. W. Hill, and S. von Goeler, *Phys. Rev. E* **52**, 1980 (1995).
- [15] V. A. Boiko, S. A. Pikuz, U. I. Safronova, and A. Ya. Faenov, *Mon. Not. R. Astron. Soc.* **185**, 789 (1978).
- [16] A. J. Smith, P. Beiersdorfer, K. Widmann, M. H. Chen, and J. H. Schofield, *Phys. Rev. A* **62**, 052717 (2000).
- [17] M. F. Gu, M. Schmidt, P. Beiersdorfer, H. Chen, D. B. Thorn, E. Trabert, E. Behar, and S. M. Kahn, *Astrophys. J.* **627**, 1066 (2005).
- [18] F. B. Rosmej, A. Ya. Faenov, T. A. Pikuz, F. Flora, P. Di Lazzaro, T. Letardi, A. Grilli, A. Reale, L. Palladino, G. Tomassetti, A. Scafati, and L. Reale, *J. Phys. B* **31**, L921 (1998).
- [19] U. I. Safronova, M. S. Safronova, and R. Bruch, *J. Phys. B* **28**, 2803 (1995).
- [20] F. Bely-Dubau, A. H. Gabriel, and S. Volonte, *Mon. Not. R. Astron. Soc.* **186**, 405 (1979).
- [21] M. H. Chen, *At. Data. Nucl. Data Tables* **34**, 301 (1986).
- [22] Y. Y. Goryayev, A. M. Urnov, and L. A. Vainshtein, [arXiv:physics/0603164](https://arxiv.org/abs/physics/0603164).
- [23] L. Natarajan, A. Natarajan, and R. Kadrekar, *Phys. Rev. A* **82**, 062514 (2010).
- [24] R. Kadrekar and L. Natarajan, *Phys. Rev. A* **84**, 062506 (2011).
- [25] R. Kadrekar and L. Natarajan, *J. Phys. B* **43**, 155001 (2010).
- [26] R. C. Elton, J. A. Cobble, H. R. Griem, D. S. Montgomery, R. C. Mancini, V. L. Jacobs, and E. Behar, *J. Quant. Spectrosc. Radiat. Transfer* **65**, 185 (2000).
- [27] F. B. Rosmej, H. R. Griem, R. C. Elton, V. L. Jacobs, J. A. Cobble, A. Ya. Faenov, T. A. Pikuz, M. Geissel, D. H. H. Hoffmann, W. Süß, D. B. Uskov, V. P. Shevelko, and R. C. Mancini, *Phys. Rev. E* **66**, 056402 (2002).
- [28] S. R. Elliott, P. Beiersdorfer, S. B. Libby, A. L. Osterheld, and T. Phillips, *Opt. Commun.* **113**, 204 (1994).
- [29] P. Jonsson, X. He, C. Froese Fischer, and I. P. Grant, *Comput. Phys. Commun.* **177**, 597 (2007).
- [30] F. A. Parpia, C. Froese Fischer, and I. P. Grant, *Comput. Phys. Commun.* **94**, 249 (1996).
- [31] I. P. Grant *et al.*, *Comput. Phys. Commun.* **21**, 207 (1980).
- [32] B. J. McKenzie, I. P. Grant, and P. H. Norrington, *Comput. Phys. Commun.* **21**, 233 (1980).
- [33] I. P. Grant, *Relativistic Quantum Theory of Atoms and Molecules: Theory and Computation* (Springer, New York, 2007).
- [34] L. Natarajan, *J. Phys. B* **35**, 3179 (2002).
- [35] NIST online bibliographic database at <http://physics.nist.gov/asd3>.